

Diffusive and hydrodynamic magnetotransport around a density perturbation in a two-dimensional electron gas

P. Shubham Parashar and Michael M. Fogler

Department of Physics, University of California, San Diego, CA 92093, USA

(Dated: January 26, 2026)

We study current flow around a circular density depletion in a two-dimensional electron gas in the presence of a strong magnetic field. The depletion is parametrized by a power-law tail with an exponent $\beta > 2$. We show that current and electrochemical potential are exponentially suppressed inside a surrounding area much larger than the geometric size of the depletion region. The corresponding “no-go” radius grows as a certain power of the magnetic field. Residual current and potential exhibit spiraling patterns inside the no-go region. Outside of it, they acquire corrections inversely proportional to the distance, which is known as the Landauer resistivity dipole. The Landauer dipole is rotated by the angle $\pi(1 - 1/\beta)$ with respect to the direction of the average electric field. We also consider the effect of electron viscosity and show that the variation of the no-go radius with magnetic field becomes more rapid if viscosity is large enough. In that regime the size of the Landauer dipole is set by the Gurzhi length, which is much larger than the no-go radius, which is in turn much larger than the geometric size of the depletion. Our results may be useful for interpreting nanoimaging of current distribution in graphene and other two-dimensional systems.

I. INTRODUCTION

Direct imaging of electron transport in two-dimensional (2D) systems has become possible recently with the development of local probes capable of

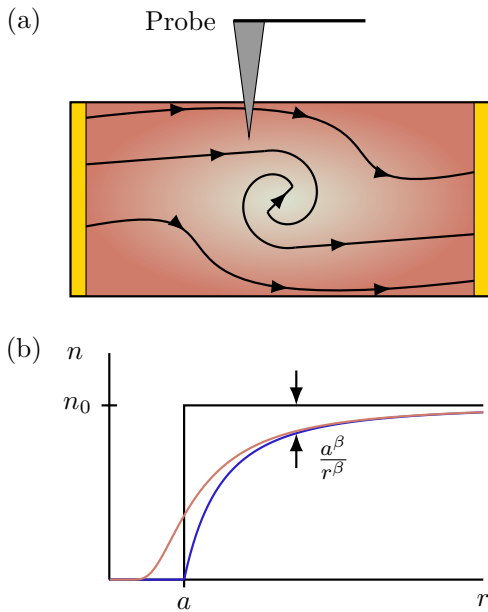


FIG. 1. (a) Schematic of the experiment that motivated this study. A local probe measures the electrochemical potential produced by a current flowing around a density depletion in a 2D electron gas. In the presence of a magnetic field, the current forms a spiral pattern around the obstacle. (b) Examples of density profiles $n(r)$ studied: abrupt (black line), smooth with a flat insulating core (blue), and smooth everywhere (red line).

nanometer-scale resolution. Scanning single-electron transistors can measure local compressibility and potential [1–4]. Subsurface charge accumulation imaging and scanning capacitance microscopy have been used to image local potentials and dissipation [5–7]. Scanning atomic force microscopy [8], scanning tunneling microscopy and potentiometry [9–11], scanning SQUID [12, 13], and nitrogen-vacancy center magnetometry [14] are also among the techniques that provide access to the distributions of the electrochemical potential $e\Phi$ and current density \mathbf{j} . Strong magnetic field has been shown to have a dramatic effect on electron transport. This regime can be defined by the condition that the Hall conductivity σ_{xy} exceeds the dissipative conductivity σ_{xx} . In particular, in the quantum Hall effect (QHE) the latter vanishes, and as a result, current can flow only along the edges. In real QHE devices, the longitudinal conductivity σ_{xx} is small but finite, so the current penetrates into the bulk [15, 16]. The current distribution is nontrivial and highly sensitive to device geometry and inhomogeneities which can be modeled by spatially varying σ_{xx} and σ_{xy} [17].

In this work, we study the current flow around a local density perturbation. It is motivated by recent scanning tunneling potentiometry (STP) experiments in graphene [18–21]. In those experiments, a local charging effect was employed to create a circular depletion region containing a p – n junction of radius 0.5 – $1.0 \mu\text{m}$. The depletion played a role of a strong obstacle for the current. The maps of the electrochemical potential $e\Phi(\mathbf{r})$, $\mathbf{r} = (x, y)$ near the junction were measured and the principal observations were as follows. Inside the depletion, $\Phi(\mathbf{r})$ had not much variation indicating that the current was blocked. The potential outside the p – n junction was fitted to the form

$$\Phi(r, \theta) \propto -x - \frac{R_L^2}{r} \cos(\theta + \theta_L), \quad (1)$$

where the first term corresponds to a uniform electric field in the $\hat{\mathbf{x}}$ -direction and the second is a correction known as the Landauer resistivity dipole [22–26]. (A 2D dipole potential behaves as $1/r$ rather than $1/r^2$ in three dimensions.) In the absence of the magnetic field, $B = 0$, the dipole had the angular orientation $\theta_L = 0$, consistent with a simple qualitative picture where the current incident on the obstacle causes charge crowding (uncrowding) on its upstream (downstream) sides. In the presence of a weak magnetic field, $B \lesssim 1$ T, the dipole rotated with respect to the asymptotic direction of the electric field: $\theta_L \neq 0$. This implies a twisted, spiral-like current flow around the depletion, Fig. 1(a). Additionally, the region where the current was suppressed grew beyond the geometric boundary of the p – n junction and acquired some spiral-like structure. These observations were analyzed using several theoretical approaches: an analytical model of diffusive transport with the hard-wall boundary condition at the p – n junction, a semiclassical ballistic correction to this model, and numerical simulations of quantum transport. The first one predicted that the Landauer dipole rotation angle is $\theta_L = 2\theta_H$ where $\theta_H = \arctan(\sigma_{xy}/\sigma_{xx})$ is the Hall angle, in agreement with the experiment. The last two approaches explained an additional feature of $\Phi(x, y)$ detected near the obstacle in strong fields $B \gtrsim 1$ T: a small kink at the distance of one cyclotron diameter away from the p – n boundary.

The hard-wall boundary condition corresponds approximately to a step-like electron density profile $n(r)$, e.g., density jumping from zero to a nonzero value at some distance $r = a$ from the center of the depletion [the black curve in Fig. 1(b)]. In this work, we improve this approximation by considering a more realistic and more general model where $n(r)$ approaches its asymptotic value n_0 gradually [the blue and red curves in Fig. 1(b)], so that the correction $n(r) - n_0$ has a power-law tail:

$$\frac{n(r)}{n_0} \simeq 1 - \left(\frac{a}{r}\right)^\beta, \quad r \gg a. \quad (2)$$

If the density depletion is induced by local doping, then according to electrostatics [27], $\beta = 3$ at large r . Other values of this exponent may be possible to realize using electrostatic doping with gate dielectrics of varying thickness or electrodes of special shape. We will assume that the power-law decrease is fast enough, $\beta > 2$. Under this condition the depletion acts as a local perturbation so that the asymptotic dipolar law [Eq. (1)] is valid.

Our analysis shows that the size R_L and the rotation angle θ_L of the Landauer resistivity dipole are qualitatively different in the step-like and the gradual density profile cases. In the latter, R_L is much larger than a and grows with B if the magnetic field is strong. This implies that even a weak density depletion can strongly repel the injected current. The size of the “no-go” region, i.e., the region where the current is strongly suppressed compared to its asymptotic value at infinity is of the order of R_{dip} rather than a and it grows with B . Remarkably, the Landauer dipole rotation angle is reduced compared to that

for the hard-wall case: $\theta_L \simeq 2\theta_H - (\pi/\beta)$.

It has been shown theoretically [28–30] that the size of the Landauer dipole is determined primarily by the so-called Gurzhi length if the electron fluid has high viscosity. This effect is related to the Stokes paradox in the context of a hydrodynamic flow around a cylinder [31, 32]. High-viscosity electron fluid can be realized in modern high-mobility 2D systems, such as semiconductor nanostructures [33–40] and graphene [14, 41–47], and also in some quasi-2D metals [48–52] where electron-electron scattering rate is much higher than electron-impurity one. Motivated by this, we examine the role of viscosity in our magnetotransport problem. We show that in the viscosity-dominated regime, the scaling of the no-go radius as a function of B is modified compared to the diffusion-dominated one: it is characterized by a significantly larger power-law exponent. The size of the Landauer dipole is given by the Gurzhi length, with a logarithmic correction, similar to the zero-field case.

The remainder of this paper is organized as follows. In Sec. II we study the diffusive regime. In Sec. III we analyze the viscous flow regime. We conclude with a brief discussion in Sec. IV. Details of the derivations are presented in the Appendix.

II. DIFFUSIVE TRANSPORT

A. Model

In the diffusive regime the current density obeys the Ohm’s law,

$$\mathbf{j}(\mathbf{r}) = \sigma_{xx}(\mathbf{r})\mathbf{E}(\mathbf{r}) - \sigma_{xy}(\mathbf{r})[\hat{\mathbf{z}} \times \mathbf{E}(\mathbf{r})]. \quad (3)$$

It is common to refer to $\mathbf{E}(\mathbf{r})$ as the electric field. However, strictly speaking, $\mathbf{E}(\mathbf{r}) = -\nabla\Phi(\mathbf{r})$ where $e\Phi(\mathbf{r}) = e\Phi_e(\mathbf{r}) + \varepsilon_F(\mathbf{r})$ is the electrochemical potential, which is the sum of the electrostatic energy per electron $e\Phi_e(\mathbf{r})$ and the local chemical potential $\varepsilon_F(\mathbf{r})$. The usual transport measurements and most of the scanned probe experiments measure $\Phi(\mathbf{r})$ rather than $\Phi_e(\mathbf{r})$.

To make the model simple, we use the Drude model for the conductivity:

$$\sigma_{xy}(\mathbf{r}) = \frac{e^2\tau_{\text{mr}}}{m} \frac{\alpha}{1 + \alpha^2} n(\mathbf{r}), \quad (4)$$

$$\sigma_{xx}(\mathbf{r}) = \alpha |\sigma_{xy}(\mathbf{r})|, \quad (5)$$

$$\alpha = \frac{1}{\omega_c\tau_{\text{mr}}}, \quad (6)$$

where m is the electron mass, $\omega_c = eB/(mc)$ is the cyclotron frequency, and τ_{mr} is the momentum-relaxation time. Typically, τ_{mr} decreases with the magnetic field as the QHE is approached. If we naively assume that $\tau_{\text{mr}} \propto B^{-\chi}$ with some $0 < \chi < 1$, then $\alpha \propto 1/B^{1-\chi}$.

The inverse of Eq. (3) is

$$\mathbf{E}(\mathbf{r}) = \rho_{xx}(\mathbf{r})\mathbf{j}(\mathbf{r}) - \rho_{xy}(\mathbf{r})[\hat{\mathbf{z}} \times \mathbf{j}(\mathbf{r})], \quad (7)$$

where

$$\rho_{xy} = -\rho_{yx} = -\frac{1}{\alpha} \frac{m}{e^2 n \tau_{\text{mr}}}, \quad \rho_{xx} = \alpha |\rho_{xy}|. \quad (8)$$

The current conservation condition $\nabla \cdot \mathbf{j}(\mathbf{r}) = 0$ yields the equation for $\Phi(\mathbf{r})$:

$$\nabla \cdot [\sigma_{xx}(\mathbf{r}) \nabla \Phi(\mathbf{r})] + [\hat{\mathbf{z}} \times \nabla \sigma_{xy}(\mathbf{r})] \cdot \nabla \Phi(\mathbf{r}) = 0. \quad (9)$$

A complementary equation can be written for the stream function $\Psi(\mathbf{r})$ defined by

$$\mathbf{j}(\mathbf{r}) = \hat{\mathbf{z}} \times \nabla \Psi(\mathbf{r}). \quad (10)$$

Using $\nabla \times \mathbf{E} = 0$, we obtain

$$\nabla \cdot [\rho_{xx}(\mathbf{r}) \nabla \Psi(\mathbf{r})] + [\hat{\mathbf{z}} \times \nabla \rho_{xy}(\mathbf{r})] \cdot \nabla \Psi(\mathbf{r}) = 0, \quad (11)$$

which has the same structure as Eq. (9). In this Section we choose to work with Eq. (9) because it is perhaps more familiar than Eq. (11) but in Sec. III we switch to the stream-function formalism.

We are mainly interested in the high-field regime $\omega_c \tau_{\text{mr}} \gg 1$, so that $\alpha \ll 1$ and $\sigma_{xx} \ll |\sigma_{xy}|$. Below we discuss exact solutions of Eq. (9) that can be found for some $n(r)$ profiles. One such example is Eq. (2) or more precisely,

$$\frac{n(r)}{n_0} = 1 - \left(\frac{a}{r}\right)^\beta, \quad r > a \quad (12)$$

supplemented with $n(r) = 0$ at $r < a$, i.e., a flat insulating core [the blue curve in Fig. 1(b)]. Another example is

$$n(r) = n_0 \exp \left[- (a/r)^\beta \right], \quad (13)$$

which has the same large-distance behavior but is smooth everywhere. Both models will be shown to give the same results for the current and potential distributions in the region of primary interest $r \gg a$.

B. Qualitative discussion

In strong magnetic fields the current tends to flow along the lines of constant $\sigma_{xy}(\mathbf{r})$. One way to understand this “Ruzin’s principle” [17] is to invoke the analogy to advection-diffusion of a passive tracer in a hydrodynamic flow. Indeed, Eq. (9) is mathematically identical to the equation that governs the steady state of a system with the diffusion constant $D = \sigma_{xx}$ and the flow velocity $\mathbf{v} = \hat{\mathbf{z}} \times \nabla \sigma_{xy}(\mathbf{r})$. The contours of constant $\sigma_{xy}(\mathbf{r})$ are the streamlines of this flow. The QHE regime $\sigma_{xx} \rightarrow 0$ corresponds to the limit of vanishing diffusion, in which the current is bound to the contours $\sigma_{xy}(\mathbf{r}) = \text{const}$. In the present case, these are concentric circles around the origin. Since these contours are closed, the transport in the bulk is impossible in the QHE regime. The current

can enter or exit the system only along the distant edges where $\sigma_{xy}(\mathbf{r})$ eventually drops to zero, so that $\nabla \sigma_{xy} \neq 0$.

The strong-field regime with small but nonzero $\sigma_{xx} \ll \sigma_{xy}$ maps to the case where some diffusion does occur, so that the tracer particles can escape from the closed orbits. This diffusive spreading is the strongest effect far away from the depletion where the velocity \mathbf{v} is small, so that it takes a long time for the tracer to drift any given length. In contrast, near the depletion, where velocity \mathbf{v} is relatively high, the tracer tends to stay on the circular orbit for many revolutions before the diffusion moves it away. In the context of magnetotransport, this suggests a picture where the lines of current are asymptotically straight at infinity where $\mathbf{j}(x, y) = \mathbf{j}_0 = \text{const}$ but become twisted and spiral-like [53] near the depletion. It also implies that there is a characteristic no-go distance R_{no} such that at $r \ll R_{\text{no}}$ the current is strongly suppressed, $|\mathbf{j}| \ll |\mathbf{j}_0|$. This no-go distance increases as σ_{xx} decreases, becoming infinite in the QHE regime.

We use the following heuristic argument to estimate R_{no} . Consider a circular streamline of some radius r . After one full revolution, the diffusion broadens the stream laterally by the distance

$$\delta(r) \sim \sqrt{2Dt}, \quad (14)$$

where $t = 2\pi r/|\mathbf{v}|$ is the travel time. If this broadening is much smaller than r , then the diffusion is ineffective, i.e., the tracer remains “locked” on the closed orbit. Therefore, we estimate the no-go radius R_{no} by requiring that the diffusive spreading is of the order of R_{no} itself:

$$\delta(R_{\text{no}}) \sim \sqrt{\frac{4\pi\alpha a}{\beta} \left(\frac{R_{\text{no}}}{a}\right)^{\beta+1} R_{\text{no}}} \sim R_{\text{no}}. \quad (15)$$

The solution of this equation scales as

$$R_{\text{no}} \sim \alpha^{-\frac{1}{\beta}} a. \quad (16)$$

It indicates that R_{no} is much larger than the geometric size a of the depletion region provided $\alpha \ll 1$. If $\alpha \propto 1/B^{1-\chi}$, then the no-go radius grows with magnetic field as a weak power-law: $R_{\text{no}} \propto B^{\frac{1-\chi}{\beta}}$.

C. Analytical solutions

We verify the above heuristic argument by solving Eq. (9) in a regular manner. Due to the rotational symmetry of the problem, the solution can be expanded in angular momentum harmonics $e^{im\theta}$. Let us assume that the electric field and current density become uniform at large r . In this case, $\Phi(\mathbf{r})$ contains only the $m = 1$ harmonic (p -wave), i.e.,

$$\Phi(r, \theta) = \Re e [\phi(r) e^{i\theta}]. \quad (17)$$

At large r , function $\phi(r)$ must have the asymptotic behavior

$$\phi(r) \simeq -r - \frac{\lambda}{r}. \quad (18)$$

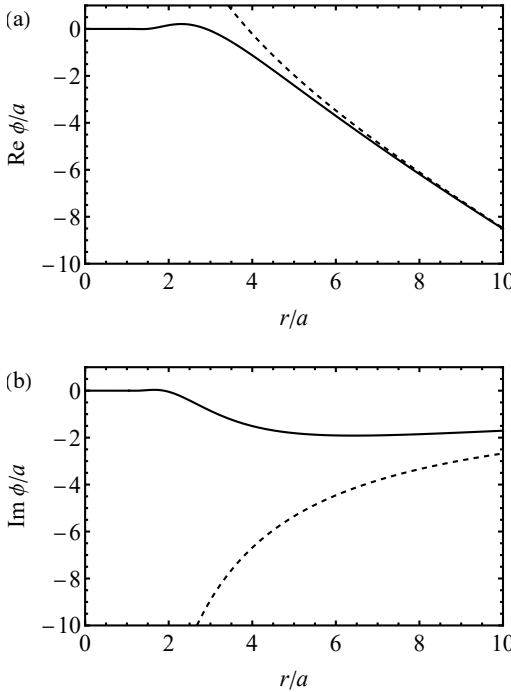


FIG. 2. (a) $\Re \phi(r)$ for $\alpha = 0.01, \beta = 3$. The solid line ($r/a \geq 1$ part) is Eq. (A6), the dashed line is Eq. (18). (b) Same for $\Im \phi(r)$.

The first term represents a uniform unit electric field. The second term, proportional to a complex number λ , describes the Landauer resistivity dipole with the size and angular orientation given by

$$R_L = |\lambda|^{1/2}, \quad \theta_L = \arg \lambda, \quad (19)$$

cf. Eqs. (1) and (19). Substituting Eq. (17) into Eq. (9), we find

$$\phi'' + \left(\frac{1}{r} + \frac{\sigma'_{xx}}{\sigma_{xx}} \right) \phi' - \left(\frac{1}{r^2} - \frac{i}{r} \frac{\sigma'_{xy}}{\sigma_{xx}} \right) \phi = 0. \quad (20)$$

In addition to Eq. (18), we need a boundary condition for short distances. For example, in the model where the conductivity vanishes at the origin [Eq. (13)], the suitable boundary condition is $\phi(0) = 0$. In the model with a finite-size insulating core, i.e., $n(r) = \sigma_{xx}(r) = \sigma_{xy}(r) = 0$ at $r \leq a$, the potential $\phi(a)$ does not have to vanish but must be bounded. (In fact, it is exponentially small if $\alpha \ll 1$, see below.) To fix $\phi(r)$ at $r < a$ one needs to make additional assumptions because Eq. (20) becomes an identity at such r . For simplicity, we choose the linear ansatz,

$$\phi(r) = \frac{r}{a} \phi(a), \quad r < a, \quad (21)$$

which corresponds to a uniform electric field of magnitude $|\phi(a)/a|$.

The exact solution of our boundary-value problem for the density profile given by Eq. (12) can be expressed in terms of the Gauss hypergeometric functions, see Eqs. (A1)–(A7) in Appendix A. The plots of the real and imaginary parts of $\phi(r)$ are shown in Fig. 2. The potential is very small at $r \lesssim 3a$, which is roughly consistent with our estimate [Eq. (16)] of the no-go radius $R_{\text{no}}(\alpha = 0.01, \beta = 3) \sim 4.6a$. At $r > R_{\text{no}}$, function $\Re \phi(r)$ becomes approximately linear whereas $\Im \phi(r)$ goes as $1/r$, in agreement with Eq. (18).

A closer look at the no-go region reveals that $\phi(r)$ has some oscillations. The period of the oscillations becomes shorter and their amplitude becomes exponentially small as r decreases. This fine structure is put on view more clearly in a false color plot of the 2D potential distribution $\Phi(x, y)$, Fig. 3. The superimposed equipotential contours are seen to spiral inward clockwise as they approach the insulating core from infinity and then spiral outward counterclockwise as they go away to infinity. (Inside the $r < a$ core, the equipotentials go across as straight lines but this is not shown in Fig. 3.) This behavior is consistent with the qualitative picture introduced in Sec. II B. Solutions exhibiting similar spiral patterns have also been discussed in Ref. [53].

In the region $r \gg a$ of primary interest we can elucidate the found exact solution by approximating it with more familiar special functions. At such r the term containing σ'_{xx} is subleading, so we can simplify Eq. (20) by dropping this term. We arrive at

$$\phi''(r) + \frac{1}{r} \phi'(r) - \left(\frac{1}{r^2} - \frac{i\beta}{\alpha} \frac{a^\beta}{r^{\beta+2}} \right) \phi(r) = 0, \quad (22)$$

which can be interpreted as a radial Schrödinger equation in the p -wave channel for a particle subject to an imaginary potential $V(r) \propto -ir^{-\beta-2}$. This equation has two linearly independent solutions, one of which expo-

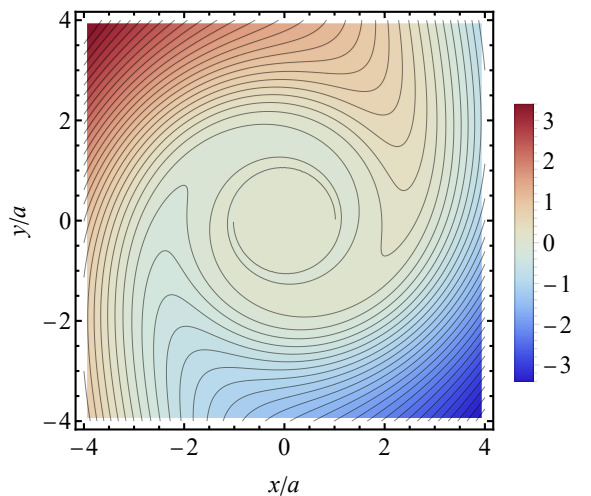


FIG. 3. False color and contour plots of the electrochemical potential $e\Phi(x, y)$ in the diffusive regime for the density profile given by Eq. (12). Parameters: $\alpha = 0.01, \beta = 3$.

nentially increases and one decreases as r approaches the origin:

$$\phi_{\pm}(r) \simeq r^{\frac{\beta}{4}} \exp\left(\pm \frac{2}{\sqrt{i\alpha\beta}} \left(\frac{a}{r}\right)^{\frac{\beta}{2}}\right), \quad r \rightarrow 0. \quad (23)$$

This asymptotic form can be derived using, e.g., the Wentzel-Kramers-Brillouin (WKB) approximation. The solution consistent with our “no-go” principle is the one with the minus sign in the argument of the exponential. The no-go radius is set by r such that this argument is of the order of unity, in agreement with Eq. (16).

The full analytical form of this approximate solution is

$$\phi(r) = -\frac{2a}{\Gamma\left(\frac{2}{\beta}\right)} \left(\frac{1}{i\alpha\beta}\right)^{\frac{1}{\beta}} K_{\frac{2}{\beta}}\left(\frac{2}{\sqrt{i\alpha\beta}} \left(\frac{a}{r}\right)^{\frac{\beta}{2}}\right), \quad (24)$$

where $K_{\nu}(x)$ is the modified Bessel function of the second kind and $\Gamma(x)$ is the Euler Gamma function. This expression is normalized to match Eq. (18) at large r . The Landauer dipole parameters extracted from this matching according to Eq. (19) are

$$\frac{R_L^2}{a^2} = \frac{\Gamma\left(1 - \frac{2}{\beta}\right)}{\Gamma\left(1 + \frac{2}{\beta}\right)} \left(\frac{1}{\alpha\beta}\right)^{\frac{2}{\beta}}, \quad \theta_L = \pi - \frac{\pi}{\beta}. \quad (25)$$

Under the assumed condition $\beta > 2$ the size R_L of the Landauer dipole is finite but at $\beta = 2$ it diverges. It can be shown that at $\beta \leq 2$ the far-field behavior of the potential no longer obeys Eq. (18): the correction $\phi(r) + r$ decays slower than $1/r$. The size of the Landauer dipole given by Eq. (25) is parametrically the same as the no-go radius:

$$R_L \sim R_{\text{no}} \sim \alpha^{-\frac{1}{\beta}} a. \quad (26)$$

In this sense, at large distances the effect of the depletion is similar to that of a hard-wall circular barrier of radius R_{no} . However, there is one curious difference. As mentioned in Sec. I, the Landauer dipole rotation angle for the hard-wall case is

$$\theta_L = \pi - 2 \arctan \alpha \simeq \pi. \quad (27)$$

Comparing Eqs. (25) and (27) we see that for the gradual density profile the angle θ_L is reduced by π/β compared to that for the hard-wall barrier.

Note that the hard-wall case can be analyzed within our formalism simply by taking the limit $\beta \rightarrow \infty$ where the density profile becomes step-like: $n(r) = 0$ at $r < a$ and $n(r) = n_0$ at $r > a$. We have checked that Eq. (27) is then fully reproduced provided we use the exact solutions of Eq. (20) rather than the small- α approximation of Eq. (24), see Appendix A.

III. HYDRODYNAMIC TRANSPORT

A. Model

We now turn to the regime where frequent electron-electron collisions endow the electron fluid with shear viscosity [54–57]

$$\nu = \frac{1}{4} \frac{v_F^2 \tau_{\text{ee}}}{1 + 4\omega_c^2 \tau_{\text{ee}}^2}, \quad (28)$$

where v_F is the Fermi velocity and τ_{ee} is the average time between collisions. (For the specific case of graphene, see also Refs. 58–61.) We focus on the range of magnetic fields such that $1/\tau_{\text{mr}} \ll \omega_c \ll 1/\tau_{\text{ee}}$ where ν is B -independent. The corresponding hierarchy of the key length scales is

$$l_{\text{ee}} \ll R_c \ll l_{\text{mr}}, \quad (29)$$

where $l_{\text{ee}} = v_F \tau_{\text{ee}}$ is the electron-electron mean free path, $R_c = v_F/\omega_c$ is the cyclotron radius, and $l_{\text{mr}} = v_F \tau_{\text{mr}}$ is the momentum-relaxation length.

Equation (7) acquires an extra viscous friction term:

$$\mathbf{E}(\mathbf{r}) = \rho_{xx}(\mathbf{r}) \mathbf{j}(\mathbf{r}) - \rho_{xy}(\mathbf{r}) [\hat{\mathbf{z}} \times \mathbf{j}(\mathbf{r})] - \frac{1}{ne} \nabla \cdot \mathbf{\Pi}(\mathbf{r}), \quad (30)$$

where $\mathbf{\Pi}$ is the viscous stress tensor [31, 32]. Its components are given by

$$\begin{aligned} \Pi_{ik} = mn\nu & \left[\nabla_i u_k + \nabla_k u_i - \frac{1}{2} \delta_{ik} (\nabla \cdot \mathbf{u}) \right] \\ & + mn\nu_B \delta_{ik} (\nabla \cdot \mathbf{u}), \end{aligned} \quad (31)$$

where \mathbf{u} is the flow velocity related to the current via

$$\mathbf{j} = en\mathbf{u}, \quad (32)$$

and ν_B is the bulk viscosity. To keep the model as simple as possible, we assume that $\nu_B + \frac{1}{2}\nu = 0$, so that the total viscous friction force is just

$$\nabla \cdot \mathbf{\Pi}(\mathbf{r}) = mn\nu \nabla^2 \mathbf{u}. \quad (33)$$

In principle, our system also possesses Hall viscosity $\nu_H = 2\nu\omega_c\tau_{\text{ee}}$ [54–57, 62–64]. Under the stated condition $\omega_c\tau_{\text{ee}} \ll 1$ we can neglect it. Our Eq. (30) [and the earlier Eq. (3) as well] also neglects the thermoelectric effect arising from the gradient of temperature T that enters the Gibbs-Duhem relation $\nabla \varepsilon_F = n\nabla p - s\nabla T$. Here s is the entropy per particle and p is the pressure. This effect should be small in a degenerate 2D electron fluid to begin with and it results in corrections that are of higher order in gradients than the terms we have kept, cf. Refs. [29, 60, 61, 65]. On the other hand, Eq. (30) does include the term ∇p appearing in the hydrodynamical equation of motion [31, 32] because \mathbf{E} is not the electric field but rather the electrochemical gradient, see Sec. II.

Requiring $\nabla \times \mathbf{E} = 0$, after some algebra, we arrive at the fourth-order partial differential equation for Ψ :

$$(1 - l_G^2 \nabla^2) \nabla \cdot (\rho_{xx} \nabla \Psi) + (\hat{\mathbf{z}} \times \nabla \rho_{xy}) \cdot \nabla \Psi = 0, \quad (34)$$

where

$$l_G = \sqrt{\nu \tau_{\text{mr}}} \sim \sqrt{l_{\text{ee}} l_{\text{mr}}} \quad (35)$$

is referred to as the Gurzhi length [66]. As we discuss below, viscosity plays an important role if $l_G \gg a$.

B. Qualitative discussion

Assuming gradients scale as $\nabla \sim 1/R_{\text{no}}$, Eq. (34) maps to the advection-diffusion equation with the diffusion coefficient and the drift velocity given by

$$D \sim \left(1 + \frac{l_G^2}{R_{\text{no}}^2}\right) \rho_{xx}, \quad \mathbf{v} = \hat{\mathbf{z}} \times \nabla \rho_{xy}, \quad (36)$$

so that Eq. (15) changes to

$$\delta(R_{\text{no}}) \sim \sqrt{\left(1 + \frac{l_G^2}{R_{\text{no}}^2}\right) \frac{\alpha a}{\beta} \left(\frac{R_{\text{no}}}{a}\right)^{\beta+1}} R_{\text{no}} \sim R_{\text{no}}. \quad (37)$$

Suppose β and $l_G \gg a$ are fixed, then as a function of α , the solution of Eq. (37) exhibits a change in behavior at $1/\alpha \sim (l_G/a)^\beta$. In stronger fields, R_{no} follows Eq. (16), with small corrections. In weaker fields, such that

$$\left(\frac{l_G}{a}\right)^2 \ll \frac{1}{\alpha} \ll \left(\frac{l_G}{a}\right)^\beta, \quad (38)$$

the no-go length obeys a power-law with a different exponent, $R_{\text{no}} \propto \alpha^{-\frac{1}{\beta-2}}$. For future convenience, we define R_{no} with a specific numerical coefficient, as follows:

$$R_{\text{no}} = \left(\frac{\beta}{\alpha} \frac{a^2}{l_G^2}\right)^{\frac{1}{\beta-2}} a = \left(\beta \frac{a^2 \omega_c}{\nu}\right)^{\frac{1}{\beta-2}} a. \quad (39)$$

In this viscosity-dominated regime, the no-go length grows as $R_{\text{no}} \propto B^{1/(\beta-2)}$. In still weaker fields, $1/\alpha \ll (l_G/a)^2$, the no-go length should be equal to the geometric size a of the depletion. This dependence is shown schematically in Fig. 4.

C. Far-field region

At large distances, the resistivities ρ_{xx} , ρ_{xy} become uniform, so that Eq. (34) reduces to

$$\nabla^2 \left[\nabla^2 \Psi(\mathbf{r}) - \frac{1}{l_G^2} \Psi(\mathbf{r}) \right] = 0. \quad (40)$$

Suppose the current is also uniform at infinity, then $\Psi(\mathbf{r})$ must be a p -wave,

$$\Psi(\mathbf{r}) = \Re \left[\psi(r) i e^{i(\theta+\theta_H)} \right], \quad (41)$$

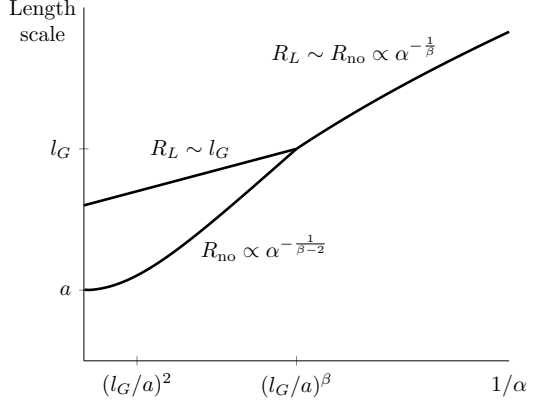


FIG. 4. A cartoon of the dependence of the no-go length R_{no} and the Landauer dipole size R_L on $1/\alpha$, i.e., the magnetic field. The crossover from the viscous regime (where $R_{\text{no}} \ll R_L$) to the diffusive regime (where $R_{\text{no}} \sim R_L$) occurs as the field increases and R_{no} (or equivalently, R_L) exceeds the Gurzhi length l_G .

with the large- r behavior

$$\psi(r) \simeq -r + \frac{\tilde{\lambda}}{r}, \quad \tilde{\lambda} \equiv \lambda e^{-2i\theta_H} \quad (42)$$

to match Eq. (18). [For simplicity, we omit the constant factor $\sqrt{\sigma_{xx}^2(\infty) + \sigma_{xy}^2(\infty)}$.] The general solution of Eqs. (40)–(42) is

$$\psi(r) = -r + \frac{\tilde{\lambda}}{r} + \mu K_1(r/l_G), \quad (43)$$

where μ is a constant. In the high viscosity limit $l_G \rightarrow \infty$, the last term behaves as $\ln r + \text{const}$, signifying the breakdown of the dipole law. This is known as the Stokes paradox [31, 32]. Since $K_1(r/l_G)$ decays exponentially at $r \gg l_G$, in the present case this paradox is moot.

The coefficients $\tilde{\lambda}$ and μ can be determined by matching Eq. (43) with the solution for $\psi(r)$ at short distances. For example, if we impose the no-slip boundary condition $\psi'(r) = \psi(r) = 0$ at some $r = a$, then [28]

$$\tilde{\lambda} = a^2 - \mu a K_1(a/l_G) = a^2 + 2a l_G \frac{K_1(a/l_G)}{K_0(a/l_G)}. \quad (44)$$

The only effect of the magnetic field is to rotate the Landauer dipole by twice the Hall angle θ_H with respect to the average electric field,

$$\lambda(B) = \lambda(0) e^{2i\theta_H(B)}, \quad (45)$$

same as for diffusive transport around a hard-wall obstacle. (However, if the Hall viscosity ν_H is retained and the boundary conditions are different from the no-slip ones [67], then there is an additional correction to θ_L of the order of $\nu_H/\nu \sim \omega_c \tau_{\text{ee}}$ [29, 30].)

If l_G is much larger than a , we can expand the Bessel functions in Eq. (44) to get

$$R_L = \left| \tilde{\lambda} \right|^{1/2} \simeq \frac{\sqrt{2}}{\sqrt{\ln(l_G/a)}} l_G. \quad (46)$$

This formula shows that an obstacle of radius a can perturb the flow at a much larger distance R_L , which is equal to the Gurzhi length reduced by a logarithmic factor. In our case, the no-slip boundary condition is effectively imposed at the no-go radius, so we expect

$$R_L^2 \simeq \frac{2l_G^2}{\ln(l_G/R_{\text{no}})}, \quad l_G \gg R_{\text{no}}. \quad (47)$$

D. Analytical approximations

Being the fourth order, the viscous hydrodynamics Eq. (34) is much more complicated than the diffusive transport one (i.e., the same equation with $l_G = 0$). We have not succeeded in finding its full analytical solutions for either of the two studied density profiles, Eqs. (12) and (13). An approximate solution can be derived if the three relevant length scales are well separated:

$$a \ll R_{\text{no}} \ll l_G \quad (48)$$

using the asymptotic matching method explained below.

First, as in Sec. II C, we can simplify the problem by treating ρ_{xx} as a constant at distances $r \gg a$. The equation for $\psi(r)$ becomes

$$(1 - l_G^2 \Delta_r) \Delta_r \psi(r) - \frac{i\beta}{\alpha} \frac{a^\beta}{r^{\beta+2}} \psi(r) = 0, \quad (49)$$

where Δ_r is the Laplacian operator in the p -wave channel:

$$\Delta_r = \frac{d^2}{dr^2} + \frac{1}{r} \frac{d}{dr} - \frac{1}{r^2}. \quad (50)$$

Next, at intermediate distances $a \ll r \ll l_G$, we can simplify Eq. (49) to

$$-\Delta_z^2 \psi - \frac{i}{z^{\beta+2}} \psi = 0, \quad z \equiv \frac{r}{R_{\text{no}}}. \quad (51)$$

This equation has four linearly independent solutions. We need to select the one that obeys the correct boundary conditions. At $z \ll 1$, i.e., $r \ll R_{\text{no}}$, the WKB approximation is valid. It predicts four possible types of asymptotic behavior:

$$\psi \sim \exp \left(-\frac{4}{\beta-2} e^{-\frac{i\pi}{8}} i^k z^{-\frac{\beta-2}{4}} \right), \quad (52)$$

depending on $k = 0, 1, 2$, or 3 . (Here i^k is a quartic root of unity.) The options $k = 0$ and 1 describe oscillations that decay exponentially as $r = R_{\text{no}}z \rightarrow 0$, so they are allowed; $k = 2$ and 3 correspond to an exponential increase, so they must be ruled out.

At distances $R_{\text{no}} \ll r \ll l_G$, the $i/z^{\beta+2}$ term in Eq. (51) can also be discarded, which yields the biharmonic equation $\Delta_z^2 \psi = 0$ with the general solution

$$\psi = \frac{c_1}{z} + c_2 z + c_3 z \ln z + c_4 z^3. \quad (53)$$

The error of this approximation is about $\psi/z^{\beta-2}$. Equation (53) must match Eq. (43) or more precisely, its expansion excluding terms of order μ/l_G^3 or smaller:

$$\psi(r) \simeq \frac{\tilde{\lambda} + \mu l_G}{r} - r + \frac{\mu}{2l_G} r \left(\ln \frac{r}{2l_G} - \frac{1}{2} + \gamma \right), \quad (54)$$

where $\gamma = 0.577\dots$ is the Euler constant. This yields

$$\mu = -\frac{2l_G}{\frac{c_2}{c_3} + \ln \frac{2l_G}{R_{\text{no}}} + \frac{1}{2} - \gamma}, \quad (55)$$

$$c_4 = 0. \quad (56)$$

If $\beta > 4$, we have one more matching condition $\tilde{\lambda} + \mu l_G = c_1 R_{\text{no}}$. If $\beta \leq 4$, we can only say

$$\tilde{\lambda} + \mu l_G = O(c_2, c_3) R_{\text{no}} \quad (57)$$

based on the above error estimate at $z \sim 1$.

In Appendix B, we study the case $\beta = 3$ in more detail and arrive at

$$\tilde{\lambda} = \frac{2l_G^2}{\ln \left(\frac{2l_G}{R_{\text{no}}} \right) + 3 - 5\gamma - \frac{i\pi}{2}} + O(R_{\text{no}}^2), \quad (58)$$

which agrees with Eq. (47). From this we can also extract the Landauer dipole orientation angle:

$$\theta_L = 2\theta_H + \arg \tilde{\lambda} \simeq 2\theta_H + \frac{\pi}{2 \ln \left(\frac{2l_G}{R_{\text{no}}} \right)}. \quad (59)$$

Hence, θ_L is larger than $2\theta_H$ in the viscous transport whereas the opposite is true in the diffusive one [Eq. (25)].

In Fig. 5 we compare these analytical predictions with numerical results (the solid line, see the figure caption). The quantity plotted is the dimensionless combination $r\delta\psi(r) \equiv r[r + \psi(r)]/R_{\text{no}}^2$ whose asymptotic value is $\tilde{\lambda}/R_{\text{no}}^2$. The numerical results behave as expected, approaching the dashed line [Eq. (43)] at large r and the dotted line [Eq. (B9)] at small r . All the lines converge together at $R_{\text{no}} \lesssim r \lesssim l_G$, validating our matching method. Given the modestly large parameter $l_G/R_{\text{no}} = 10$ used in this calculation, the agreement can be considered very good, especially for the real part of the stream function, Fig. 5(a). To improve the agreement for the imaginary part, we chose the second term in Eq. (58) to be $-3iR_{\text{no}}^2$, which is 12% of the total $\Im \tilde{\lambda}$.

In Fig. 6 we show the 2D plots of the stream function at intermediate distances $a \ll r \lesssim l_G$. The zoomed-in view of the no-go region [Fig. 6(b)] reveals spiral-like pattern of the current flow, similar to the diffusive case, Fig. 3.

IV. DISCUSSION

In this study, motivated by recent STP experiments [21], we examined a 2D magnetotransport around an inhomogeneity in the form of a circular-symmetric depletion with a power-law electron density profile. We confined ourselves to the case where the exponent $\beta > 2$ of this power law is sufficiently large, so that this disturbance belongs to the class of local perturbations. We modeled the transport by both diffusive and hydrodynamic equations. The main qualitative result is that in strong magnetic fields the current is repelled away from the depletion region to distances much greater than its characteristic geometric size. The corresponding “no-go” radius increases with magnetic field. It follows the power law with a small exponent $(1 - \chi)/\beta$ in the diffusive case and a larger exponent $1/(\beta - 2)$ in the hydrodynamic case. The crossover between the two scaling laws occurs when the no-go radius reaches the Gurzhi length.

The exponentially small current inside the no-go re-

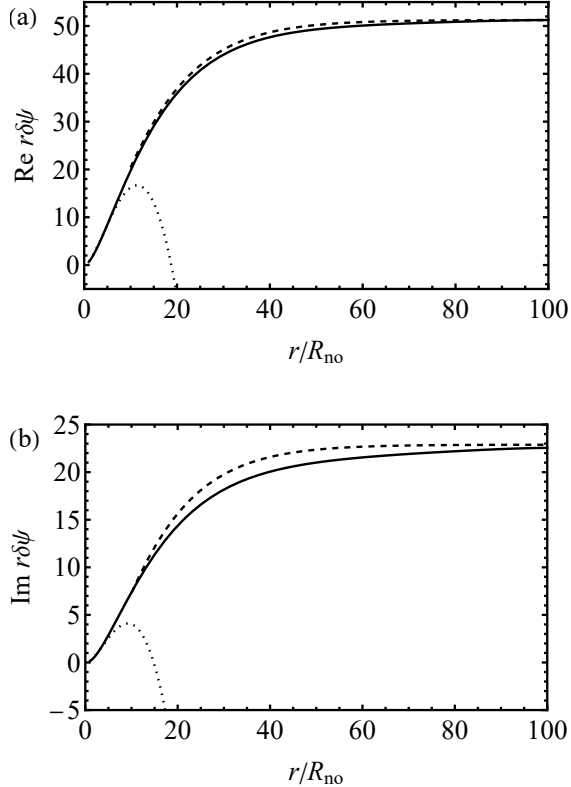


FIG. 5. Analytical and numerical results for the stream function. The panels (a) and (b) depict, respectively, the real and imaginary parts of $r\delta\psi(r) \equiv r[r + \psi(r)]/R_{\text{no}}^2$ that approaches $\tilde{\lambda}/R_{\text{no}}^2 = 51.2 + 22.9i$ at large r . The solid line is the numerical solution of Eq. (49) with the boundary conditions $\psi(r_{\min}) = \psi'(r_{\min}) = 0$, $\psi(r_{\max}) = -r_{\max} + \tilde{\lambda}/r_{\max}$, $\psi'(r_{\max}) = -1 - \tilde{\lambda}/r_{\max}^2$. The dotted line is obtained from Eq. (B9); the dashed line (plotted for $r > l_G$) is from Eqs. (43), (55), (58). Parameters: $\beta = 3$, $l_G/R_{\text{no}} = 10$, $r_{\min}/R_{\text{no}} = 0.1$, $r_{\max}/R_{\text{no}} = 100$.

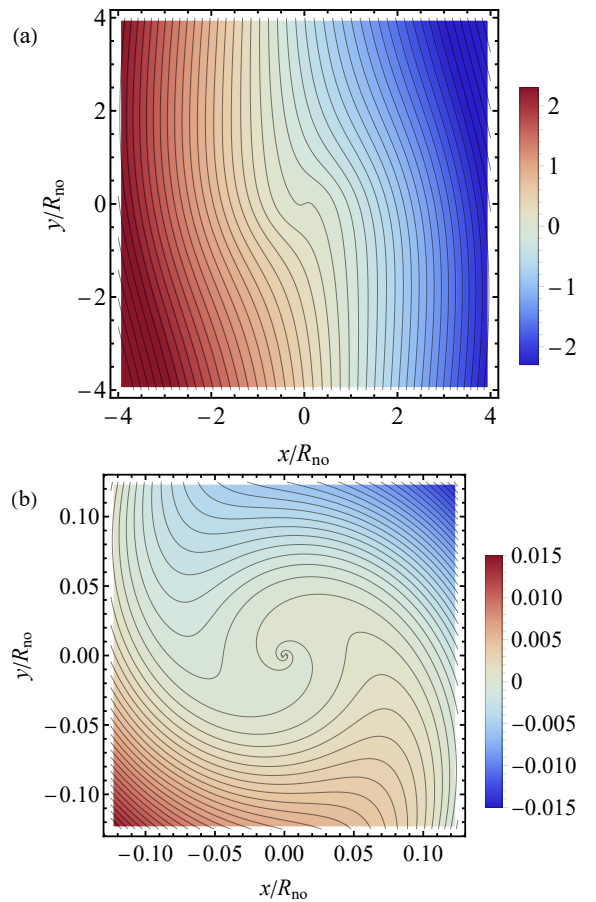


FIG. 6. False color and contour plots of the stream function in the viscous regime for $\beta = 3$, $l_G/R_{\text{no}} = 10$. (a) $\Psi(x, y)$ computed using Eq. (B9). (b) Enlarged view of the no-go region, using Eq. (B11).

gion exhibits an intriguing spiral pattern. The spiraling is driven by the Lorentz force gradient, so it has a different origin from vortical flow that can arise in viscous hydrodynamics [41, 52, 68–70] even in the absence of the magnetic field. The twisting of the current lines at short distances has an effect on the asymptotic behavior. It changes the angular orientation of the Landauer dipole, i.e., the correction to the uniform current at large distances.

The Landauer dipole and the effective obstacle size we have investigated are the simplest and the most robust characteristics. They can be extracted already from STP maps collected at a moderate resolution. By varying B and tracking how the no-go radius grows, one can in principle distinguish diffusive and hydrodynamic behavior and estimate the electron viscosity. High-resolution scans [21] have been shown to also resolve a small anomaly of the electrochemical potential predicted to occur [71, 72] at the distance of one cyclotron diameter $2R_c$ from the hard-wall barrier. In this regard, our classical continuum medium theory has a number of limitations. Both the diffusive and the hydrodynamic ap-

proximations become inaccurate at short distances. They do not account for features on the scale of the cyclotron radius where the motion is ballistic. These approaches also fail at low temperatures and long distances, where quantum localization — the hallmark of the QHE — becomes important. To remedy these shortcomings, self-consistent solutions of the Boltzmann kinetic equation and quantum transport simulations in a realistic potential profile may be necessary. The scaling rules we have derived may provide a useful reference for these more ambitious calculations.

ACKNOWLEDGEMENTS

We are grateful to Z. Krebs and V. Brar for prior collaboration on Ref. [21] that inspired this study.

Appendix A: Exact solutions for the diffusive transport

For the density profile Eq. (12), Eq. (20) can be solved in terms of the Gauss hypergeometric function, which is a particular case of the generalized hypergeometric function [73]

$${}_pF_q \left(\begin{matrix} a_1, \dots, a_p \\ b_1, \dots, b_q \end{matrix} \middle| x \right).$$

There are two linearly independent solutions, $f_{\pm}(r)$:

$$f_{\pm}(r) = \left(\frac{r}{a} \right)^{\frac{1}{2}\beta c_{\pm}} {}_2F_1 \left(\begin{matrix} a_{\pm}, b_{\pm} \\ c_{\pm} \end{matrix} \middle| \frac{r^{\beta}}{a^{\beta}} \right), \quad (\text{A1})$$

$$a_{\pm} = \frac{1}{2} - \frac{1}{\beta} \pm \kappa, \quad (\text{A2})$$

$$b_{\pm} = \frac{1}{2} + \frac{1}{\beta} \pm \kappa, \quad (\text{A3})$$

$$c_{\pm} = 1 \pm 2\kappa, \quad (\text{A4})$$

$$\kappa = \frac{\sqrt{(4 + \beta^2)\alpha^2 + 4i\alpha\beta}}{2\alpha\beta}. \quad (\text{A5})$$

The solution that satisfies the proper boundary conditions is their linear combination

$$\phi(r) = C_+ f_+(r) + C_- f_-(r), \quad r > a, \quad (\text{A6})$$

with the coefficients

$$C_{\pm} = -\frac{\Gamma(\pm 2\kappa)}{\Gamma\left(\frac{2}{\beta}\right)} \frac{\Gamma(b_{\mp})}{\Gamma(a_{\pm})} a. \quad (\text{A7})$$

Expanding $\phi(r)$ at large r , we find the expression for λ :

$$\frac{\lambda}{a^2} = -\frac{\Gamma\left(1 - \frac{2}{\beta}\right)}{\Gamma\left(1 + \frac{2}{\beta}\right)} \frac{\Gamma(b_+) \Gamma(b_-)}{\Gamma(a_+) \Gamma(a_-)}. \quad (\text{A8})$$

This formula can be simplified in the two limits discussed in the main text. For small α and finite β , we get

$$\frac{\lambda}{a^2} = -\frac{\Gamma\left(1 - \frac{2}{\beta}\right)}{\Gamma\left(1 + \frac{2}{\beta}\right)} \left(\frac{1}{i\alpha\beta} \right)^{\frac{2}{\beta}}, \quad \alpha \ll 1, \frac{1}{\beta}, \quad (\text{A9})$$

in agreement with Eq. (25). For an arbitrary α and infinite β , we get

$$\lim_{\beta \rightarrow \infty} \lambda = -\frac{1 - i\alpha}{1 + i\alpha} a^2, \quad (\text{A10})$$

which matches Eq. (27).

For the density profile of Eq. (13), we find the solution for $\phi(r)$ in terms of the Kummer confluent hypergeometric function:

$$\begin{aligned} \phi(r) = & -r {}_1F_1 \left(\begin{matrix} -\frac{1}{\beta} - \frac{i}{\alpha\beta} \\ 1 - \frac{2}{\beta} \end{matrix} \middle| \frac{a^{\beta}}{r^{\beta}} \right) \\ & - \frac{\lambda}{r} {}_1F_1 \left(\begin{matrix} \frac{1}{\beta} - \frac{i}{\alpha\beta} \\ 1 + \frac{2}{\beta} \end{matrix} \middle| \frac{a^{\beta}}{r^{\beta}} \right), \end{aligned} \quad (\text{A11})$$

where λ is given by

$$\lambda = -\frac{\Gamma\left(1 - \frac{2}{\beta}\right)}{\Gamma\left(1 + \frac{2}{\beta}\right)} \frac{\Gamma\left(-\frac{i}{\alpha\beta} + \frac{1}{\beta}\right)}{\Gamma\left(-\frac{i}{\alpha\beta} - \frac{1}{\beta}\right)} a^2. \quad (\text{A12})$$

This equation agrees with Eqs. (A9) and (A10) in the limits indicated. This confirms that the short-range details of the density profile are unimportant if the no-go radius is much larger than a .

Appendix B: Solutions for the viscous hydrodynamic transport

The four linearly independent solutions of Eq. (51) with $\beta = 3$ are

$$\psi_1(r) = \frac{1}{z} {}_0F_3 \left(\begin{matrix} - \\ 3, 3, 5 \end{matrix} \middle| -\frac{i}{z} \right), \quad (\text{B1})$$

$$\psi_2(r) = G_{0,4}^{2,0} \left(\begin{matrix} - \\ -1, 1; -3, -1 \end{matrix} \middle| -\frac{i}{z} \right), \quad (\text{B2})$$

$$\psi_3(r) = G_{0,4}^{3,0} \left(\begin{matrix} - \\ -1, -1, 1; -3 \end{matrix} \middle| +\frac{i}{z} \right), \quad (\text{B3})$$

$$\psi_4(r) = G_{0,4}^{4,0} \left(\begin{matrix} - \\ -3, -1, -1, 1; \end{matrix} \middle| -\frac{i}{z} \right), \quad (\text{B4})$$

where

$$G_{pq}^{mn} \left(\begin{matrix} a_1, \dots, a_p \\ b_1, \dots, b_q \end{matrix} \middle| x \right)$$

is the Meijer G -function [73] and

$$z = \frac{\alpha}{3} \frac{l_G^2}{a^3} r = \frac{r}{R_{\text{no}}}. \quad (\text{B5})$$

The small- r asymptotic behavior of these functions is given by Eq. (52):

$$\psi(r) \sim \exp \left[-4e^{-\frac{i\pi}{8}} i^k \left(\frac{R_{\text{no}}}{r} \right)^{\frac{1}{4}} \right]. \quad (\text{B6})$$

Functions $\psi_1(r)$ and $\psi_2(r)$ are exponentially increasing as $r \rightarrow 0$, so they are not allowed. Functions $\psi_3(r)$ and $\psi_4(r)$ correspond, respectively, to $k = 1$ and 0, i.e., the slower and the faster exponential decay. We need to examine them further. At large r , we find

$$\psi_3(r) \simeq -\frac{i}{2} \left(\ln z + \frac{5}{2} - 4\gamma - \frac{i\pi}{2} \right) z, \quad (\text{B7})$$

$$\psi_4(r) \simeq -6iz^3. \quad (\text{B8})$$

Therefore, we must discard $\psi_4(r)$ and keep $\psi_3(r)$ only. The properly normalized expression is

$$\psi(r) = i \frac{R_{\text{no}}}{l_G} \mu \psi_3(z) \quad (\text{B9})$$

and the ratio c_2/c_3 needed for Eq. (58) is

$$\frac{c_2}{c_3} = \frac{5}{2} - 4\gamma - \frac{i\pi}{2}. \quad (\text{B10})$$

The higher-accuracy asymptotic formula for $\psi_3(r)$ used in making Fig. 6(b) is

$$\begin{aligned} \psi_3(zR_{\text{no}}) &= e^{-\frac{9i\pi}{16}} \sqrt{\frac{\pi}{2}} \left(1 + \frac{123}{32} e^{-\frac{5i\pi}{8}} z^{\frac{1}{4}} \right) \\ &\times z^{11/8} \exp \left(-4e^{\frac{3i\pi}{8}} z^{-\frac{1}{4}} \right). \end{aligned} \quad (\text{B11})$$

[1] A. Yacoby, H. Hess, T. Fulton, L. Pfeiffer, and K. West, *Solid State Communications* **111**, 1 (1999).

[2] J. Martin, N. Akerman, G. Ulbricht, T. Lohmann, J. H. Smet, K. von Klitzing, and A. Yacoby, *Nature Physics* **4**, 144 (2007).

[3] S. Ilani, J. Martin, E. Teitelbaum, J. H. Smet, D. Mahalu, V. Umansky, and A. Yacoby, *Nature* **427**, 328 (2004).

[4] C. Kumar, J. Birkbeck, J. A. Sulpizio, D. Perello, T. Taniguchi, K. Watanabe, O. Reuven, T. Scaffidi, A. Stern, A. K. Geim, and S. Ilani, *Nature* **609**, 276 (2022).

[5] S. H. Tessmer, P. I. Glicofridis, R. C. Ashoori, L. S. Levitov, and M. R. Melloch, *Nature* **392**, 51 (1998).

[6] G. Finkelstein, P. Glicofridis, S. Tessmer, R. Ashoori, and M. R. Melloch, *Physical Review B* **61**, R16323 (2000).

[7] M. E. Suddards, A. Baumgartner, M. Henini, and C. J. Mellor, *New Journal of Physics* **14**, 083015 (2012).

[8] K. L. McCormick, M. T. Woodside, M. Huang, M. Wu, P. L. McEuen, C. Duruoz, and J. S. Harris, *Physical Review B* **59**, 4654 (1999).

[9] P. Muralt and D. W. Pohl, *Applied Physics Letters* **48**, 514 (1986).

[10] K. Hashimoto, C. Sohrmann, J. Wiebe, T. Inaoka, F. Meier, Y. Hirayama, R. A. Römer, R. Wiesendanger, and M. Morgenstern, *Physical Review Letters* **101**, 256802 (2008).

[11] G. Li, A. Luican-Mayer, D. Abanin, L. Levitov, and E. Y. Andrei, *Nature Communications* **4**, 10.1038/ncomms2767 (2013).

[12] A. Uri, Y. Kim, K. Bagani, C. K. Lewandowski, S. Grover, N. Auerbach, E. O. Lachman, Y. Myasoedov, T. Taniguchi, K. Watanabe, J. Smet, and E. Zeldov, *Nature Physics* **16**, 164 (2019).

[13] A. Uri, S. Grover, Y. Cao, J. Crosse, K. Bagani, D. Rodan-Legrain, Y. Myasoedov, K. Watanabe, T. Taniguchi, P. Moon, M. Koshino, P. Jarillo-Herrero, and E. Zeldov, *Nature* **581**, 47 (2020).

[14] J. A. Sulpizio, L. Ella, A. Rozen, J. Birkbeck, D. J. Perello, D. Dutta, M. Ben-Shalom, T. Taniguchi, K. Watanabe, T. Holder, *et al.*, *Nature* **576**, 75 (2019).

[15] R. W. Rendell and S. M. Girvin, *Phys. Rev. B* **23**, 6610 (1981).

[16] A. H. MacDonald, T. M. Rice, and W. F. Brinkman, *Physical Review B* **28**, 3648 (1983).

[17] I. M. Ruzin, *Physical Review B* **47**, 15727 (1993).

[18] P. Willke, T. Kotzott, T. Pruschke, and M. Wenderoth, *Nature Communications* **8**, 10.1038/ncomms15283 (2017).

[19] W. A. Behn, Z. J. Krebs, K. J. Smith, K. Watanabe, T. Taniguchi, and V. W. Brar, *Nano Letters* **21**, 5013 (2021).

[20] Z. J. Krebs, W. A. Behn, S. Li, K. J. Smith, K. Watanabe, T. Taniguchi, A. Levchenko, and V. W. Brar, *Science* **379**, 671 (2023).

[21] Z. J. Krebs, W. A. Behn, K. J. Smith, M. A. Fortman, K. Watanabe, T. Taniguchi, P. S. Parashar, M. M. Fogler, and V. W. Brar **10.48550/ARXIV.2409.19468** (2024), [arXiv:2409.19468](https://arxiv.org/abs/2409.19468).

[22] R. Landauer, *IBM Journal of Research and Development* **1**, 223 (1957).

[23] R. Landauer, *Zeitschrift für Physik B Condensed Matter and Quanta* **21**, 247 (1975).

[24] R. S. Sorbello, *Physical Review B* **23**, 5119 (1981).

[25] W. Zwerger, L. Bönig, and K. Schönhammer, *Physical Review B* **43**, 6434 (1991).

[26] M. Reuß and W. Zwerger, *Physical Review B* **53**, 9513 (1996).

[27] M. M. Fogler, D. S. Novikov, and B. I. Shklovskii, *Physical Review B* **76**, 233402 (2007).

[28] A. Lucas, *Physical Review B* **95**, 115425 (2017).

[29] I. V. Gornyi and D. G. Polyakov, *Physical Review B* **108**, 165429 (2023).

[30] P. S. Alekseev and A. P. Dmitriev, *Physical Review B* **108**, 205413 (2023).

[31] H. Lamb, *Hydrodynamics*, republ. of the 6th ed., Cambridge 1932 ed. (Dover, New York, 2005).

[32] L. D. Landau and E. M. Lifshitz, *Fluid Mechanics* (Butterworth-Heinemann, London, 1987).

[33] L. W. Molenkamp and M. J. M. de Jong, *Physical Review B* **49**, 5038 (1994).

[34] M. J. M. de Jong and L. W. Molenkamp, *Physical Review B* **51**, 13389 (1995).

[35] A. D. Levin, G. M. Gusev, E. V. Levinson, Z. D. Kvon, and A. K. Bakarov, *Physical Review B* **97**, 245308 (2018).

[36] G. M. Gusev, A. D. Levin, E. V. Levinson, and A. K. Bakarov, *Physical Review B* **98**, 161303 (2018).

[37] G. M. Gusev, A. S. Jaroshevich, A. D. Levin, Z. D. Kvon, and A. K. Bakarov, *Scientific Reports* **10**, 10.1038/s41598-020-64807-6 (2020).

[38] A. Gupta, J. Heremans, G. Kataria, M. Chandra, S. Falahai, G. Gardner, and M. Manfra, *Physical Review Letters* **126**, 076803 (2021).

[39] A. C. Keser, D. Q. Wang, O. Klochan, D. Y. Ho, O. A. Tkachenko, V. A. Tkachenko, D. Culcer, S. Adam, I. Farer, D. A. Ritchie, O. P. Sushkov, and A. R. Hamilton, *Physical Review X* **11**, 031030 (2021).

[40] X. Wang, P. Jia, R.-R. Du, L. N. Pfeiffer, K. W. Baldwin, and K. W. West, *Physical Review B* **106**, L241302 (2022).

[41] D. Bandurin, I. Torre, R. K. Kumar, M. Ben Shalom, A. Tomadin, A. Principi, G. Auton, E. Khestanova, K. Novoselov, I. Grigorieva, *et al.*, *Science* **351**, 1055 (2016).

[42] J. Crossno, J. K. Shi, K. Wang, X. Liu, A. Harzheim, A. Lucas, S. Sachdev, P. Kim, T. Taniguchi, K. Watanabe, T. A. Ohki, and K. C. Fong, *Science* **351**, 1058 (2016).

[43] R. Krishna Kumar, D. A. Bandurin, F. M. D. Pellegrino, Y. Cao, A. Principi, H. Guo, G. Auton, M. Ben Shalom, L. A. Ponomarenko, G. Falkovich, K. Watanabe, T. Taniguchi, I. Grigorieva, L. S. Levitov, M. Polini, and A. Geim, *Nature Physics* **13**, 1182 (2017).

[44] D. A. Bandurin, A. V. Shytov, L. S. Levitov, R. K. Kumar, A. I. Berdyugin, M. Ben Shalom, I. V. Grigorieva, A. K. Geim, and G. Falkovich, *Nature Communications* **9**, 10.1038/s41467-018-07004-4 (2018).

[45] A. I. Berdyugin, S. G. Xu, F. M. D. Pellegrino, R. Krishna Kumar, A. Principi, I. Torre, M. Ben Shalom, T. Taniguchi, K. Watanabe, I. V. Grigorieva, M. Polini, A. K. Geim, and D. A. Bandurin, *Science* **364**, 162 (2019).

[46] M. J. H. Ku, T. X. Zhou, Q. Li, Y. J. Shin, J. K. Shi, C. Burch, L. E. Anderson, A. T. Pierce, Y. Xie, A. Hamo, U. Vool, H. Zhang, F. Casola, T. Taniguchi, K. Watanabe, M. M. Fogler, P. Kim, A. Yacoby, and R. L. Walsworth, *Nature* **583**, 537 (2020).

[47] J. Geurs, Y. Kim, K. Watanabe, T. Taniguchi, P. Moon, and J. H. Smet, *arXiv:2008.04862* (2020).

[48] P. J. W. Moll, P. Kushwaha, N. Nandi, B. Schmidt, and A. P. Mackenzie, *Science* **351**, 1061 (2016).

[49] M. D. Bachmann, A. L. Sharpe, G. Baker, A. W. Barnard, C. Putzke, T. Scaffidi, N. Nandi, P. H. McGuinness, E. Zhakina, M. Moravec, S. Khim, M. König, D. Goldhaber-Gordon, D. A. Bonn, A. P. Mackenzie, and P. J. W. Moll, *Nature Physics* **18**, 819 (2022).

[50] J. Gooth, F. Menges, N. Kumar, V. Süß, C. Shekhar, Y. Sun, U. Drechsler, R. Zierold, C. Felser, and B. Gotsmann, *Nature Communications* **9**, 10.1038/s41467-018-06688-y (2018).

[51] U. Vool, A. Hamo, G. Varnavides, Y. Wang, T. X. Zhou, N. Kumar, Y. Dovzhenko, Z. Qiu, C. A. C. Garcia, A. T. Pierce, J. Gooth, P. Anikeeva, C. Felser, P. Narang, and A. Yacoby, *Nature Physics* **17**, 1216 (2021).

[52] A. Aharon-Steinberg, T. Völk, A. Kaplan, A. K. Pariari, I. Roy, T. Holder, Y. Wolf, A. Y. Meltzer, Y. Myasoedov, M. E. Huber, *et al.*, *Nature* **607**, 74 (2022).

[53] M. M. Fogler and B. I. Shklovskii, *Solid State Communications* **94**, 503 (1995).

[54] S. Chapman and T. G. Cowling, *The Mathematical theory of non-uniform gases*, 3rd ed. (Cambridge University, Cambridge, 1999).

[55] M. S. Steinberg, *Physical Review* **109**, 1486 (1958).

[56] A. N. Kaufman, *The Physics of Fluids* **3**, 610 (1960).

[57] P. Alekseev, *Physical Review Letters* **117**, 166601 (2016).

[58] A. Principi, G. Vignale, M. Carrega, and M. Polini, *Physical Review B* **93**, 125410 (2016).

[59] B. N. Narozhny, I. V. Gornyi, A. D. Mirlin, and J. Schmalian, *Annalen der Physik* **529**, 10.1002/andp.201700043 (2017).

[60] A. Lucas and K. C. Fong, *Journal of Physics: Condensed Matter* **30**, 053001 (2018).

[61] Z. Sun, D. N. Basov, and M. M. Fogler, *Proceedings of the National Academy of Sciences* **115**, 3285 (2018).

[62] B. Bradlyn, M. Goldstein, and N. Read, *Physical Review B* **86**, 245309 (2012).

[63] C. Hoyos and D. T. Son, *Physical Review Letters* **108**, 066805 (2012).

[64] T. Holder, R. Queiroz, and A. Stern, *Physical Review Letters* **123**, 106801 (2019).

[65] A. V. Andreev, S. A. Kivelson, and B. Spivak, *Physical Review Letters* **106**, 256804 (2011).

[66] R. N. Gurzhi, *Sov. Phys. Usp.* **11**, 255 (1968).

[67] E. I. Kiselev and J. Schmalian, *Physical Review B* **99**, 035430 (2019).

[68] H. K. Moffatt, *Journal of Fluid Mechanics* **18**, 1 (1964).

[69] L. Levitov and G. Falkovich, *Phys. Rev. Lett.* **117**, 026601 (2016).

[70] G. Falkovich and L. Levitov, *Physical Review Letters* **119**, 066601 (2017).

[71] T. Holder, R. Queiroz, T. Scaffidi, N. Silberstein, A. Rozen, J. A. Sulpizio, L. Ella, S. Ilani, and A. Stern, *Physical Review B* **100**, 245305 (2019).

[72] O. E. Raichev, G. M. Gusev, A. D. Levin, and A. K. Bakarov, *Physical Review B* **101**, 235314 (2020).

[73] F. W. J. Olver, D. W. Lozier, R. F. Boisvert, and C. W. Clark, *NIST Digital library of mathematical functions* (2010).